Evaluation of Maximum-Likelihood based Attenuation Correction in Positron Emission Tomography[1]

J. Nuyts[2], *Member, IEEE*, P. Dupont[2], S.Stroobants[2], A. Maes[2], L. Mortelmans[2], P. Suetens, *Member, IEEE*[3].

[2]Nuclear Medicine, K.U.Leuven, B3000 Leuven, Belgium

[3]ESAT-PSI, K.U.Leuven, B3000 Leuven, Belgium

Abstract

In positron emission tomography, transmission scans are used to correct the acquired data for the effect of photon attenuation. The noise present in the transmission measurement often has a significant effect on the signal to noise ratio of the final attenuation corrected image of the tracer distribution.

This study evaluates the effect of different attenuation correction strategies on the performance of human observers in a tumor detection task. The four strategies considered are: no attenuation correction, multiplication with the count ratio of blank and transmission sinograms, reprojection of a maximum-likelihood reconstruction, and reprojection of a maximum-a-posteriori reconstruction of the transmission sinogram. Performance in tumor detection was quantified as the contrast at which the number of errors increased beyond 20%. No statistically significant difference was found between classical attenuation correction and maximum-likelihood based correction. With maximum-a-posteriori based attenuation correction performance was significantly better than with the other methods.

I. Introduction

Several authors have reported that maximum-likelihood (ML) and maximum-a-posteriori (MAP) reconstruction leads to high quality reconstructions, both in emission and transmission tomography [1, 2, 3]. ML-algorithms have been mainly used in emission tomography, but there is an increasing interest in its application for transmission tomography. However, in particular for transmission tomography, there is still a need for careful quantitative measurement of the effect of such algorithms on diagnostic accuracy.

An important application of ML-reconstruction of transmission scans is in the computation of attenuation correction factors in PET. Currently, PET is often used in combination with ^{18}F-fluorodeoxyglucose (FDG) for oncological examinations. In many cases, the aim is the detection of possible metastases, the presence of which may have a significant effect on further treatment. Since tracer accumulation tends to be increased in the tumor tissue, the tumor is imaged as a hot spot. Therefore, we have designed an experiment to evaluate the influence of ML-based attenuation correction on tumor detection by human observers.

[1]This work is supported by the Flemish Fund for Scientific Research (FWO), grant number G.0106.98. P. Dupont is post-doctoral researcher of the FWO.

II. Attenuation correction algorithms

In this study four attenuation correction strategies have been compared. The strategies are applied to two-dimensional sinograms (dimensions: detector position and projection angle).

The first strategy is to simply ignore attenuation, a strategy often applied in clinical practice to avoid the lengthy transmission study.

The second strategy is to apply the classical attenuation correction technique:

$$A_i^c = \frac{(\vec{s} \otimes \vec{b})_i}{(\vec{s} \otimes \vec{y})_i} \tag{1}$$

where A_i^c is the attenuation correction factor for sinogram pixel i, $\vec{b}$ is the blank sinogram, $\vec{y}$ is the measured transmission sinogram, $\vec{s}$ is a two-dimensional Gaussian smoothing kernel and $\otimes$ denotes convolution. It is assumed that the blank sinogram has been scaled to compensate for differences in acquisition time. Smoothing is required to suppress the noise in the transmission sinogram, but excessive smoothing results in artifacts [4].

The third strategy is to compute the attenuation correction factors by reprojecting a reconstruction of the attenuation image. This approach ensures that the attenuation correction factors form a consistent set, implying that some noise has been removed. When done with filtered backprojection (FBP), the noise on the resulting attenuation correction factors decreases significantly, but the effect on the attenuation corrected images is very small [5]. McKee et al. [6] derived an approximate expression for the signal to noise ratio in the reconstructed emission image, predicting no noise suppression when attenuation correction factors are produced by reprojection from FBP. The reason is that the noise removed by reprojection from FBP would also have been removed by applying FBP to the emission data corrected with "raw" attenuation correction factors. The derivation assumes noise-free emission data and a uniform transmission sinogram, but even when these conditions are not met, reprojection from FBP is not very effective [7].

However, ML reconstruction can be expected to have a marked effect, since it deals with noise in a different way, taking into account the Poisson nature of the transmission data. ML-based attenuation correction factors were computed as

follows.

$$A_i^m = \exp\left((\vec{s} \otimes \sum_j c_{\cdot j}\mu_j)_i\right) \quad (2)$$

$$\mu_j^{\text{new}} = \mu_j + \frac{\alpha}{N}\left(1 - \frac{\sum_i c_{ij} y_i}{\sum_i c_{ij} b_i a_i}\right) \quad (3)$$

$$a_i = \exp\left(-\sum_\xi c_{i\xi}\mu_\xi\right) \quad (4)$$

Here, c_{ij} is the relative contribution of pixel j to the projection value of sinogram pixel i, $\vec{\mu}$ is the reconstructed attenuation image, N is the number of rows or columns in the reconstruction and α is a relaxation factor. Equation (3) represents a single iteration from our gradient ascent maximum-likelihood algorithm for transmission tomography [7, 8, 9]. Fessler et al. [10] derived a class of algorithms for transmission tomography with proven convergence under ideal conditions, and identified the convex algorithm proposed by Lange et al. [11] as a member of that class. It turns out that the algorithm (3) with $\alpha = 1$ converges to another member of that class (eq (34) in [10]) close to the solution. In the few tests we carried out, convergences rate of algorithm (3) and Lange's convex algorithm were similar.

The fourth strategy is to compute the attenuation correction factors by forward projecting a MAP reconstruction of the transmission data:

$$A_i^p = \exp\left((\vec{s} \otimes \sum_j c_{\cdot j}\mu_j)_i\right) \quad (5)$$

$$\mu_j^{\text{new}} = \mu_j + \alpha\frac{\sum_i c_{ij} a_i b_i - \sum_i c_{ij} y_i + \frac{\partial M(\vec{\mu})}{\partial \mu_j}}{N\sum_i c_{ij} a_i b_i - \alpha\frac{\partial^2 M(\vec{\mu})}{\partial \mu_j^2}} \quad (6)$$

The prior distribution M combines an a-priori distribution of absolute attenuation coefficients and a smoothing prior. The prior of attenuation coefficients was a four-modal distribution, with peaks at 0.095 cm^{-1} (combining soft tissue and bone), 0.032 and 0.019 cm^{-1} (lung tissue) and 0 cm^{-1} (air). The two modes for the lung counteract excessive smoothing in the lungs (which are very inhomogeneous in reality). For the Gibbs prior the function proposed by Geman and McClure [12] was used, to avoid smoothing over strong edges. The weights of both priors (the hyperparameters) have been determined empirically using a few independent simulations and were kept constant for the simulations presented here. Several other priors with similar features have been reported in the literature [3, 10, 13, 14].

For the iterative methods, computations were accelerated using the ordered subsets method [15]. Because noise propagation tends to increase with increasing number of subsets, we used a scheme with a gradually decreasing number of subsets, finishing with a few true ML iterations. A high number of iterations was applied to obtain "effective convergence", with good resolution near the tumor in the lungs. For the ML-method (3) the equivalent of 200 unaccelerated iterations were applied. For the MAP-method (6), which converges faster, this number was 128. In both cases, the relaxation coefficient α was set to 1.

For the methods (1),(2) and (5) a single parameter remains: the width (full width at halve maximum) of the Gaussian smoothing kernel s. In the experiments described below, we used values of 0, 4.8, 8 mm and 13 mm for the classical method and the ML-method. For the MAP-method, only the widths 0, 4.8 and 8 mm were applied: the prior suppresses high frequency noise, so there is no need for excessive smoothing. Together with the non-attenuation corrected strategy, this resulted in 12 different methods.

III. Experiments

A. Importance of the noise model

It is well known that FBP-reconstructed transmission images suffer from streak artifacts when the measurement statistics are low. In a first experiment, the importance of the inclusion of an accurate noise model into the reconstruction algorithm has been verified. From a Shepp-Logan type object, the transmission sinogram $\vec{y}$ was computed and Poisson noise was added. A noise-free blank sinogram $\vec{b}$ was assumed. Three different reconstruction images were computed. 1) FBP of the sinogram $\vec{t}$, computed as $t_i = \ln(b_i/y_i)$. 2) Maximum-likelihood expectation maximization (MLEM) for emission tomography [16] applied to t_i. This is theoretically not exact, since MLEM assumes Poisson noise on the sinogram, and $\vec{t}$ does not obey Poisson statistics. However, MLEM is known to be a robust algorithm. 3) ML-reconstruction for transmission tomography (eq 3), applied to $\vec{y}$ and $\vec{b}$.

B. Effect on attenuation correction

The effect of each of the 12 methods on tumor detection was assessed by quantifying the performance of 6 human observers in a tumor detection task. PET transmission and emission images have been simulated. The 12 methods were applied to compute 12 different sets of attenuation correction factors. The attenuation corrected emission sinograms were reconstructed with FBP. In this work, we have not studied the effect of using MLEM for the emission reconstruction.

1) Simulations

A pair of two-dimensional attenuation and activity distributions was derived from a registered set of CT and PET ^{18}F-FDG images from the same patient [17, 18]. In this pair, the PET image had been resampled to the CT pixel size. A slice through the thorax was selected.

An attenuation phantom (at CT-resolution: 0.82 mm pixel size) was created by manually editing the CT slice to compensate for truncation near the arms, and replacing the Hounsfield units with appropriate linear attenuation coefficients for 511 KeV. This was done by linearly scaling the Hounsfield units such that the resulting average soft tissue attenuation was 0.095 cm^{-1}. Consequently, the simulated attenuation map showed a realistic inhomogeneity.

To create the activity distribution with the same resolution, the CT image was thresholded in order to separate bone, soft tissue, fat, lung and air. The resulting regions were copied to the PET image and the mean tracer uptake in each of the regions was determined. An activity phantom was created by assuming that tracer uptake in each of the regions was homogeneous and equal to the mean value obtained from the PET scan. Resulting lung to soft tissue activity ratio was 0.71.

Sixteen versions of the phantom were produced by introducing a single tumor at 16 different positions, all located near the right lateral thoracic wall. Eight of those were in the right lung, the eight others in the soft tissue. Attenuation maps were adapted accordingly, since tumor attenuation was assumed to be equal to average soft tissue attenuation. Size of the tumor in the slice was 1 cm^2. The attenuation and activity distributions with all 16 tumors are shown in figure 1. The difference between activity in tumor and background was

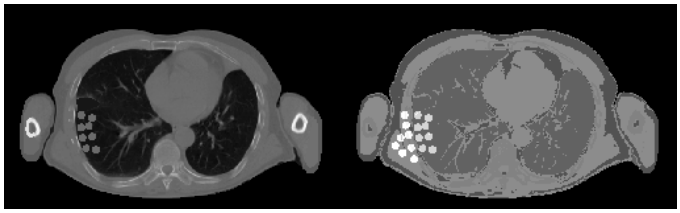

Figure 1: The software phantom: attenuation (left) and activity (right) distributions. All 16 tumors are shown, in each simulation only one of these tumors is present.

decreased from 3 times soft tissue activity to 0.34 times soft tissue activity in 31 steps using a factor of 0.93.

$$\text{act}_{\text{tumor}} = \text{act}_{\text{backg}} + 3 \times 0.93^i \times \text{act}_{\text{tissue}}, i = 0 \ldots 30 \quad (7)$$

Here, i is the contrast index and *backg* corresponds to lung or soft tissue. Defining contrast as tumor to background activity ratio, the contrast decreases in soft tissue from 4 to 1.34, while the corresponding contrasts in lung are slightly higher because the background is lower. For each contrast index, eight different images were produced, four with a lung tumor and four with a soft tissue tumor, such that all sixteen tumor positions were present in the images for two consecutive contrasts. This results in 248 images for each method. Sinograms were computed with a resolution of 0.82 mm and afterwards rebinned into matrices of 150 pixels $\times$ 256 angles with a pixel size of 3.3 mm. The sinograms were smoothed to simulate a resolution of 5 mm for the transmission and 6 mm for the emission scans. Noise was superimposed using a pseudo-random generator with Poisson characteristics, and assuming a total of 3.2×10^6 incident counts for the transmission scan (which would have been measured in absence of attenuation), and 2.4×10^6 counts for the emission scan. These values are similar to an 8 minute transmission scan and a 15 min emission scan on our 2D PET camera. The final emission sinograms were corrected for attenuation using each of the 12 methods, and reconstructed with filtered backprojection without low-pass filter.

2) User interface

An interactive program was written to evaluate tumor detection performance. A separate interactive session was performed for each attenuation correction method. The program presented all the images from a single method to the observer in order of decreasing tumor-to-background contrast. The eight images with the same contrast index were presented in random order. The observer could adjust the width of a 2D Gaussian convolution mask applied during image display, select the zoom factor, and chose the lookup table and select its parameters. The observer specified the tumor position by a mouse click. When performance decreased below a threshold the session was terminated. Each time the eight images for a particular contrast had been scored, the observer was informed about the number of wrong answers.

Starting with easily detectable tumors effectively introduces a learning phase, during which the observer learns where to look for the tumors and what artifacts may show up with the particular attenuation correction method. It also allows terminating the session when contrast has become too low, avoiding to waste time detecting invisible tumors. Since there are 16 possible tumor positions, the probability of obtaining 3 or more correct answers in eight images by guessing is about 1 %, so the procedure was expected to allow accurate measurement of performance as a measure of contrast. "Real time" smoothing eliminates the filtering of the emission images as a parameter. The fact that the observer knows that exactly one tumor is present eliminates all higher level image interpretation or thresholding by the observer. This is an advantage, since if some thresholding is applied, the threshold must be made explicit and must be varied over a large range in a receiver operating characteristic analysis. Making this mental threshold explicit is difficult and errors in doing so lead to increased variability.

3) Statistical analysis.

From each session the fraction of correct answers as a function of decreasing contrast was extracted. This function was median filtered to obtain a curve decreasing nearly monotonically from 1 to about 0.25. The point where the curve dropped below 0.8 was used as the measure of performance (this threshold was judged to yield reproducable results in a few test sessions). Thus, the outcome of the experiment is reduced to a matrix of twelve rows (the methods) and six columns (the observations). Analysis of variance for repeated measurements with Scheffé post-hoc testing was applied, $p < 0.05$ was considered significant.

IV. Results

A. Importance of the noise model

Figure 2 shows the reference image and the reconstructions with FBP, MLEM for emission and ML gradient ascent for transmission. For the ML-methods, 200 iterations were applied. As could be expected, the log-likelihood was systematically higher for the ML-gradient ascent image than

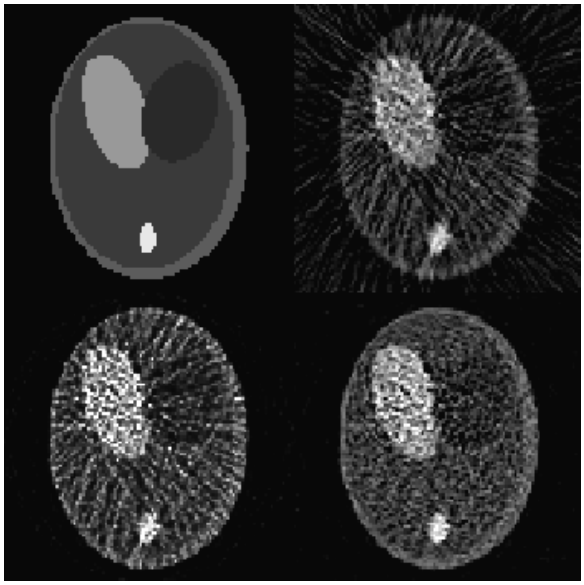

Figure 2: Reconstructions of a simulated transmission sinogram. *Top-left:* original image, *top right:* FBP, *bottom left:* MLEM for emission and *bottom right:* ML-gradient ascent for transmission.

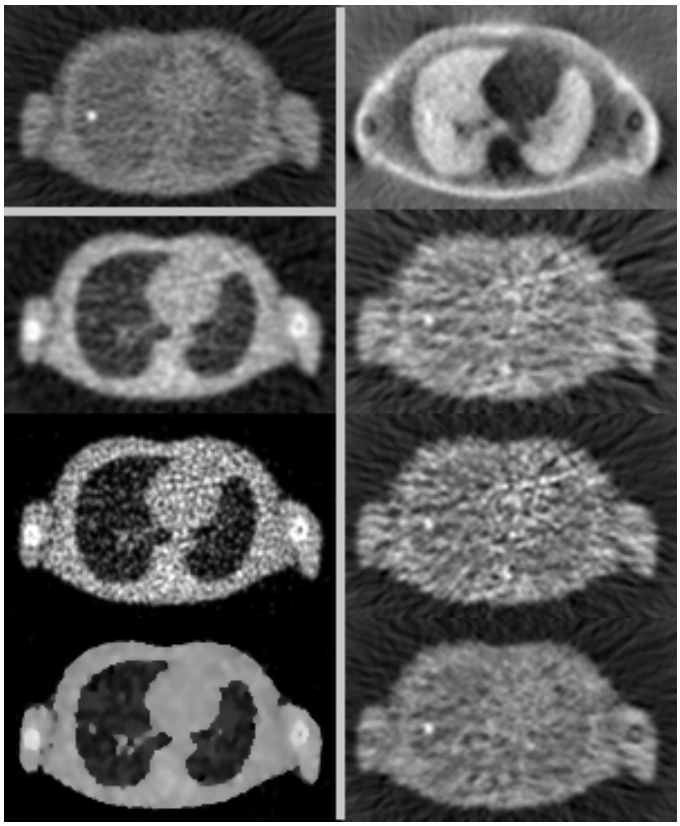

Figure 3: *Top left* FBP reconstruction with noise-free attenuation correction. *Right, from top to bottom:* FBP reconstruction without attenuation correction, with classical correction (8 mm smoothing), with ML-based correction (0 mm smoothing) and with MAP-based correction (0 mm smoothing). *Left:* FBP, ML and MAP reconstructions of the transmission sinogram.

for the MLEM image at the same iteration number. Both the FBP and MLEM image suffer from streak artifacts, which are not present in the ML-gradient ascent image. This suggests that using the appropriate noise model has a significant effect on the resulting image.

B. Effect on attenuation correction

Figure 3 shows some typical images obtained with the different methods.

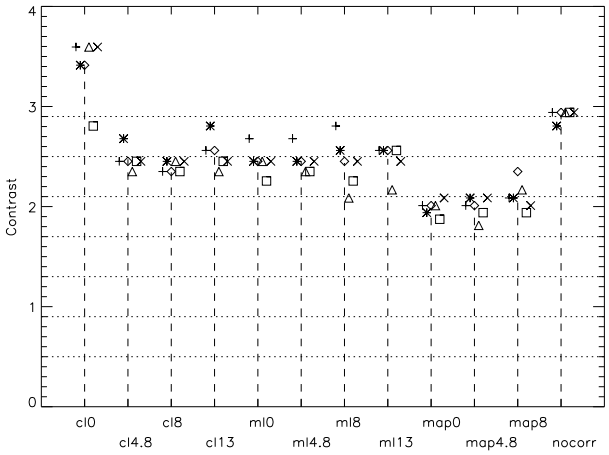

Figure 4: Contrast (tumor to tissue activity ratio) of 80% performance obtained by the observers for each of the methods. Each symbol corresponds to a single observer. The method is indicated as "cl" (classical), "ML", "MAP" and "nocorr" (no attenuation correction), followed by the width of the smoothing mask. Lower contrast indicates better performance.

Figure 4 plots the performance measures (contrast at 80% performance) for the six observers and the twelve methods. For all observers, a single session required less than 10 minutes.

Analysis of variance for repeated measurements indicated that significant differences were present ($p = 6 \times 10^{-5}$). The results of Scheffé post-hoc analysis are tabulated in table 1, significant p-values are printed in bold.

V. Discussion

The main conclusions from figure 4 and table 1 are that

- Maximum-likelihood based attenuation correction does not improve tumor detection performance when compared to the classical approach.
- Maximum-a-posteriori based attenuation correction significantly improves tumor detection relative to all other methods.

The first experiment shows that ML reconstruction for transmission produces attenuation maps with fewer artifacts, when compared to FBP or MLEM reconstruction of the log-converted data. We attributed this to the use of an appropriate noise model. Since separation of noise and signal seems superior for the ML-gradient ascent reconstruction, reprojection of this reconstruction was expected to improve

Table 1
Scheffé post-hoc analysis, evaluating if the performance differences shown in figure 4 are significant. Methods are denoted as in figure 4. Threshold was set at $p < 0.05$, smaller p-values are in bold.

	Classic				ML-method				MAP-method			no corr
FWHM mm	0	4.8	8	13	0	4.8	8	13	0	4.8	8	-
cl 0	-	**0.048**	**0.011**	0.074	**0.002**	**0.014**	0.068	0.134	**0.000**	**0.004**	**0.003**	0.442
cl 4.8	**0.048**	-	0.984	0.878	1.000	1.000	1.000	1.000	**0.029**	**0.004**	0.234	0.072
cl 8	**0.011**	0.984	-	0.939	1.000	1.000	1.000	1.000	**0.005**	**0.045**	0.282	**0.004**
cl 13	0.074	0.878	0.939	-	1.000	0.999	0.994	1.000	**0.037**	**0.003**	0.155	0.261
ml 0	**0.002**	1.000	1.000	1.000	-	1.000	1.000	1.000	**0.004**	**0.043**	0.142	0.054
ml 4.8	**0.014**	1.000	1.000	0.999	1.000	-	1.000	1.000	**0.009**	**0.015**	0.211	**0.032**
ml 8	0.068	1.000	1.000	0.994	1.000	1.000	-	1.000	0.189	**0.034**	0.677	0.363
ml 13	0.134	1.000	1.000	1.000	1.000	1.000	1.000	-	0.088	**0.004**	0.389	0.174
map 0	**0.000**	**0.029**	**0.005**	**0.037**	**0.004**	**0.009**	0.189	0.088	-	1.000	0.878	**0.000**
map 4.8	**0.004**	**0.004**	**0.045**	**0.003**	**0.043**	**0.015**	**0.034**	**0.004**	1.000	-	0.989	**0.004**
map 8	**0.003**	0.234	0.282	0.155	0.142	0.211	0.677	0.389	0.878	0.989	-	**0.009**
no corr	0.442	0.072	**0.004**	0.261	0.054	**0.032**	0.363	0.174	**0.000**	**0.004**	**0.009**	-

the attenuation correction factors. Yet, the second experiment did not reveal a performance difference between ML-based attenuation correction and the classical method (which uses the noisy raw data). A possible explanation is that the ML method trades in streaks (which are not compatible with the model) for high frequency pointwise noise (which is allowed by the model). This noise propagates into the emission image; finding a hot spot in this high frequency noise is still difficult.

Figure 4 also shows that not applying attenuation correction results in a performance worse than that obtained with any other method (except for the classical method without smoothing, never used in clinical practice). This is in apparent contrast to findings of Stroobants et al. [19] in mediastinal staging of non-small cell lung cancer, and Imran et al. [20] in a patient group with various tumors, who reported no difference in tumor detection. However, the mediastinum is a region of homogeneous attenuation, rather different from the location used in our experiment. The study by Imran et al was restricted to lesions detected in X-CT scans and scintigrams, which may not have formed a sufficiently challenging data set to find the performance difference observed in our simulation study. Bengel et al. [21] and Imran et al. [20] reported an increased tissue to background ratio in uncorrected images. Note, however, that tumor detection performance is proportional to signal to noise ratio rather than to tumor to background ratio. In non-attenuation corrected images, the background is artifactually decreased and is often even close to zero, but the noise is still present.

Separate analysis of our data for lung tumors and for soft tissue tumors (data not shown) indicated that observer performance was lower for lung tumors than for soft tissue tumors. In soft tissue, the performance of the three MAP methods was similar to that of the classical and ML methods with strong smoothing. The classical and ML methods with low smoothing resulted in poorer performance, similar to that of applying no correction. Separating the data resulted in relatively small data sets, the performance differences were not significant. The observed tendencies seem to confirm that performance differences are lower in regions of homogeneous attenuation because smoothing is more effective, and may explain the different findings reported by Stroobants et al. [19].

Consequently, overall observer performance was dominated by detection of small dense lung tumors. Attenuation correction may increase contrast in these tumors, because it compensates for the self-attenuation of the tumor, which is much higher than that of the surrounding lung tissue. The simulation represents a somewhat extreme case, though, because some lung tumors have a density lower than soft tissue (e.g. broncheo-alveolar cell carcinoma), and because breathing may reduce the resolution of the transmission scan, rendering attenuation correction less effective. Consequently, performance differences are expected to be somewhat smaller when tested in a heterogeneous patient group.

MAP based attenuation correction resulted in best tumor detection performance for both tumor types. The Gibbs prior allows smoothing of homogeneous regions, while preserving important image detail such as small dense regions in the lung. This approach actually combines reconstruction and segmentation. Several authors have used segmentation of FBP-reconstructed attenuation maps as a strategy to strongly reduce noise in the attenuation correction factors [22, 23, 24]. Incorporating the segmentation into the reconstruction has the additional advantage that the segmentation result is checked against the original unprocessed data, reducing the risk of segmentation errors.

VI. Conclusion

Our simulation indicates that maximum-a-posteriori based attenuation correction has a beneficial effect on tumor detection, when compared to other attenuation correction methods or no attenuation correction.

VII. References

[1] K.Lange, R.Carson. "EM reconstruction algorithms for emission and transmission tomography," *J. Comput. Assist. Tomogr., vol. 8, 1984,* pp. 306-316.

[2] S.H.Manglos, G.M.Gagne, A.Krol, F.D.Thomas, R.Narayanaswamy. "Transmission maximum-likelihood reconstruction with ordered subsets for cone beam CT," *Phys. Med. Biol., vol. 40, 1995,* pp. 1225-1241.

[3] E.Ü.Mumcuoğlu, R.M.Leahy, S.R.Cherry. "Bayesian reconstruction of PET images: methodology and performance analysis," *Phys. Med. Biol., vol. 41, 1996,* pp. 1777-1807.

[4] A. Chatziioannou, M. Dahlbom. "Detailed investigation of transmission and emission data smoothing protocols and their effects on emission images." *IEEE Trans. Nucl. Sci., vol. 43, 1996,* pp. 290-294.

[5] JM Ollinger. "Reconstruction-reprojection processing of transmission scans and the variance of PET images," *IEEE Trans. Nucl. Sci., vol. 39, 1992,* pp. 1122-1125

[6] BTA McKee, LG Hiltz, PJ Harvey. "Signal-to-noise ratios for attenuation correction in PET imaging," *IEEE Trans. Med. Imaging, vol. 13, 1994,*, pp. 711-715

[7] J Nuyts, P Dupont, S Vleugels, B Bertels, H Spooren, C Schiepers, L Mortelmans. "Improved image quality in PET using ML-reconstruction of low count transmission data," *Eur. J. Nucl. Med., vol. 22, 1995,* p 876.

[8] J.Nuyts, P.Dupont, L.Mortelmans. "Iterative reconstruction of transmission sinograms with low signal to noise ratio." in "2nd IEEE Workshop CMP: can we beat the curse of dimensionality (Prague, Czech Republic, Aug. 28-30, 1996)", *Birkhäuser, 1997, pp. 237-248*

[9] J.Nuyts, B.De Man, P.Dupont, M.Defrise, P.Suetens, L.Mortelmans. "Iterative reconstruction for helical CT: a simulation study," *Phys. Med. Biol., vol. 43, 1998,* pp. 729-737.

[10] Fessler JA, Ficaro EP, Clinthorne NH, Lange K 1997. "Grouped-coordinate ascent algorithms for penalized-likelihood transmission image reconstruction," *IEEE Trans. Med. Imaging vol. 16, 1997,* pp 166-175.

[11] K. Lange, J. Fessler. "Globally convergent algorithms for maximum a posteriori transmission tomography". *IEEE Trans. Image Processing, vol. 4, 1995,* pp 1430-1438.

[12] S. Geman, D.E. McClure. "Statistical methods for tomographic image reconstruction." *Bull. Int. Stat. Inst. vol. 52-4, 1987,* pp. 5-21.

[13] Z Liang, R Jaszczak, R Coleman, V Johnson. "Simultaneous reconstruction, segmentation and edge enhancement of relatively piecewise continuous images with intensity-level information." *Med. Phys., vol 18 1991,* pp. 394-401.

[14] S. Alenius, U. Ruotsalainen. "Bayesian image reconstruction for emission tomography based on median root prior," *Eur. J. Nucl. Med., vol. 24, 1997,* pp 258-265.

[15] H.M. Hudson, R.S. Larkin. "Accelerated image reconstruction using ordered subsets of projection data," *IEEE Trans. Med. Imaging, vol. 13, 1994,* pp 601-609.

[16] LS Shepp, Y Vardi. "Maximum likelihood reconstruction for emission tomography," *IEEE Trans Med Imaging,* vol MI-1, pp. 113-122, 1982.

[17] F. Maes, A. Collignon, D. Vandermeulen, G. Marchal, P. Suetens. "Multimodality image registration by maximization of mutual information," *IEEE Trans. Med. Imaging, vol. 16, 1997,* pp 187-198.

[18] J.F. Vansteenkiste, S.G. Stroobants, P.J. Dupont, P.R. De Leyn, W.F. De Wever, E.K. Verbeken, J.L. Nuyts, F.B. Mals, J.G. Bogaerts. "FDG-PET scan in potentially operable non-small cell lung cancer: do anatometabolic fusion images improve the localisation of regional lymph node metastases?". *Eur. J. Nucl. Med., vol. 25, 1998,* pp 1495-1501.

[19] S Stroobants, OS Hoekstra, P Dupont, J Vansteenkiste, E Comans, P De Leyn, J Verschakelen, M Demedts, L Mortelmans. "Mediastinal staging in NSCLC: comparison of different acquisition and reconstruction protocols." *Eur. J. Nucl. Med., vol. 24, 1997,* p 924.

[20] M.B. Imran, K. Kubota, S. Yamada, H. Fukuda, K. Yamada, T Fujiwara, M. Itoh. "Lesion-to-background ratio in nonattenuation corrected whole-body FDG PET images." *J. Nucl. Med., vol. 39, 1998,* pp 1219-1223.

[21] F.M. Bengel, S.I. Ziegler, N. Avril W. Weber, C. Laubenbacher, M. Schwaiger. "Whole-body positron emission tomography in clinical oncology: comparison between attenuation-corrected and uncorrected images." *Eur. J. Nucl. Med., vol. 24, 1997,* pp 1091-1098.

[22] SR Meikle, M Dahlbom, SR Cherry. "Attenuation correction using count-limited transmission data in positron emission tomography," *J Nucl Med, vol. 34, 1993,* pp 143-144.

[23] Y.-C. Tai, K.-P. Lin, M. Dahlbom, E.J. Hoffman. "A hybrid attenuation correction technique to compensate for lung density in 3D total body PET." *IEEE Trans. Nucl. Sci., vol. 43, 1996,* pp 323-330.

[24] M. Xu, P.D. Cutler, W.K. Luk. "Adaptive, segmented attenuation correction for whole-body PET imaging." *IEEE Trans. Nucl. Sci., vol. 43, 1996,* pp 331-336.